SI Appendix

Mechanistic insights into the interactions of NAP1 with the SKICH domains of NDP52 and TAX1BP1

Tao Fu, Jianping Liu, Yingli Wang, Xingqiao Xie, Shichen Hu, and Lifeng Pan*

SI Results

Biochemical mapping the interacting regions of NDP52 and NAP1. To validate and define the precise binding regions of NDP52 and NAP1, we carried out a quantitative isothermal titration calorimetry (ITC)-based assay using the entire NDP52 SKICH region (residues 1-126) and three different NAP1 fragments, NAP1(1-85), NAP1(1-75) and NAP1(33-75). Our result demonstrated that the three NAP1 fragments bind to NDP52(1-126) with similar *K*d values, about 1.49 μM, 1.80 μM and 1.15 μM, respectively (***SI Appendix***, **Fig. S2*A-C***), indicating that the NDP52 SKICH region indeed can directly bind to the NAP1 N-terminal coiled-coil region, and the NDP52-binding site of NAP1 is located within the NAP1(33-75) fragment. Unfortunately, our initial attempts to obtain protein crystals using the purified NDP52(1-126)/NAP1(33-75) complex failed, therefore we sought to further narrow down the NAP1-binding region of NDP52 in order to get a more suitable protein complex for subsequent structural characterizations.

Based on sequence conservation and secondary structure prediction of NDP52 (***SI Appendix***, **Fig. S1*B*)**, we constructed two additional NDP52 fragments, NDP52(10-126) and NDP52(21-126), which lack different extreme N-terminal loop residues in compare with the NDP52(1-126) fragment. Further NMR-based analysis showed that the well-dispersed ^{1}H-^{15}N HSQC spectra of those three NDP52 fragments are very similar (***SI Appendix***, **Fig. S2*D*)**, suggesting that those three NDP52 proteins are well-folded and adopt a similar overall structure. However, in contrast to NDP52(10-126), which binds to NAP1(33-75) with an affinity comparable to that of NDP52(1-126) (**Fig. 1*B*** and ***SI Appendix***, **Fig. S2*C*)**, the NDP52(21-126) fragment displays a much weaker binding affinity towards NAP1(33-75) as indicated by our ITC-based analyses (**Fig. 1*B*** and ***SI***

Appendix, **Fig. S2*E*)**. Thus, the NDP52(10-126) fragment rather than the NDP52(21-126) fragment is sufficient for binding to NAP1. To further confirm this notion, we also used NMR spectroscopy to characterize the interactions of NAP1(33-75) with NDP52(10-126) and NDP52(21-126). Titrations of ^{15}N-labeled NDP52(10-126) and NDP52(21-126) with un-labeled NAP1(33-75) proteins showed that a select set of peaks in the ^{1}H-^{15}N HSQC spectra of NDP52(10-126) and NDP52(21-126) underwent significant peak-broadenings or chemical shift changes (***SI Appendix***, **Fig. S2*F*** and ***G***), indicating that those two NDP52 proteins can directly bind to NAP1(33-75). However, further detailed analyses revealed that many peaks in the ^{1}H-^{15}N HSQC spectra of these two proteins (***SI Appendix***, **Fig. S2*F*** and ***G***), such as the peak corresponding to the V116 residue, showed very different change profiles when titrated with NAP1(33-75), and importantly, a slow exchange pattern was observed in the NMR titration experiment of NDP52(10-126) (***SI Appendix***, **Fig. S2*H***), confirming that the NDP52(10-126) and NDP52(21-126) fragments differentially bind to NAP1(33-75), and NDP52(10-126) interacts with NAP1(33-75) more strongly than the NDP52(21-126) fragment.

SI Materials and Methods

Protein expression and purification. Different DNA fragments encoding human NDP52, NAP1, TAX1BP1 and other related DNA fragments were amplified by PCR from the full-length human cDNA, respectively. All these fragments were either cloned into the pET-32M vector (a modified version of pET32a vector containing a N-terminal Trx-tag and His_6-tag) or the pET-GST vector (a modified version of pET32a vector containing a N-terminal GST-tag) for recombinant protein expressions. For the

fluorescence imaging experiment or co-immunoprecipitation assay, the full-length NDP52 and NAP1 DNA fragments were cloned into pmCherry-C1 and pEGFP-C1 vectors, respectively. All the point mutations of NDP52 and NAP1 or other relevant mutations used in this study were created using the standard PCR-based mutagenesis method, further checked by PCR screen using 2×Taq Master Mix (Vazyme Biotech Co., Ltd.) enzyme and confirmed by DNA sequencing.

Recombinant proteins were expressed in BL21 (DE3) *E. coli* cells induced by 100 μM IPTG at 16 °C. The bacterial cell pellets were re-suspended in the binding buffer (50 mM Tris, 500 mM NaCl, 5 mM imidazole at pH 7.9), and then lysed by the FB-110XNANO homogenizer machine (Shanghai Litu Machinery Equipment Engineering Co., Ltd.). Then the lysis was centrifuged at 35000g for 30 minutes to remove the debris. His_6-tagged proteins were purified by Ni^{2+}-NTA agarose (GE Healthcare) affinity chromatography, while GST-tagged proteins were purified by glutathione sepharose 4B (GE Healthcare) affinity chromatography. Each recombinant protein was further purified by size-exclusion chromatography or mono-Q ion-exchange chromatography. The N-terminal tag of each recombinant protein was cleaved by 3C protease and further removed by size-exclusion chromatography. Uniformly ^{15}N- or $^{15}N/^{13}C$-labeled proteins were prepared by growing bacteria in M9 minimal medium using $^{15}NH_4Cl$ (Cambridge Isotope Laboratories Inc., NLM-467) as the sole nitrogen source or $^{15}NH_4Cl$ and $^{13}C_6$-glucose (Cambridge Isotope Laboratories Inc., CLM-1396) as the sole nitrogen and carbon sources, respectively.

Isothermal titration calorimetry assay. ITC measurements were carried out on a MicroCal PEAQ-ITC calorimeter or an automated system (Malvern) at 25 °C. All protein samples were in the same buffer containing 20 mM Tris (pH 7.5), 100 mM NaCl and 1 mM DTT. The titration processes were performed by injecting 40 µl aliquots of the syringe sample into the cell sample at time intervals of 2 minutes to ensure that the titration peak returned to the baseline. The titration data were analyzed using the Malvern MicroCal PEAQ-ITC analysis program.

NMR spectroscopy. The stable isotope labeled protein samples for NMR studies were concentrated to ~0.1 mM for titration experiments and ~0.6 mM for backbone resonance assignment experiments in 50 mM potassium phosphate buffer containing 50 mM NaCl, and 1 mM DTT at pH 6.5. NMR spectra were acquired at 25 °C on an Agilent 800 MHz spectrometer equipped with an actively z gradient shielded triple resonance cryogenic probe. Backbone resonance assignments of the NDP52(10-126) fragment were achieved using a suite of hetero-nuclear correlation experiments including HNCO, HNCA, CA(CO)NH, HNCACB and CBCA(CO)NH using a $^{15}N/^{13}C$-labeled protein sample together with a 3D ^{15}N-seperated NOESY (1).

Analytical gel filtration chromatography. Analytical gel filtration chromatography was carried out on an AKTA FPLC system (GE Healthcare). Protein samples were loaded on to a Superose^{TM} 12 10/300 GL column (GE Healthcare) equilibrated with a buffer containing 20 mM Tris-HCl (pH 7.5), 100 mM NaCl and 1 mM DTT.

Analytical Ultracentrifugation. Sedimentation velocity experiments were performed on a Beckman XL-I analytical ultracentrifuge equipped with an eight-cell rotor under 42000 rpm at 20 °C. The partial specific volume of different protein samples and the buffer density were calculated using the program SEDNTERP (http://www.rasmb.bbri.org/). The final sedimentation velocity data were analyzed and fitted to a continuous sedimentation coefficient distribution model using the program SEDFIT (2). The fitting results are further output to the Origin 9.0 software and aligned with each other.

Protein crystallization and structural elucidation. Crystals of NDP52(10-126), NDP52(10-126)/NAP1(33-75) complex and TAX1BP1(1-121)/NAP1(33-75) complex were obtained using the sitting-drop vapor-diffusion method at 16 °C. Specifically, the freshly purified NDP52(10-126) protein (20 or 10 mg/ml in 20 mM Tris-HCl, 100 mM NaCl, 1 mM DTT, 1 mM EDTA at pH 7.5) was mixed with equal volume of reservoir solution containing 0.2 M potassium sulfate (pH 6.7), 20% (w/v) polyethylene glycol 3350. While, crystals of NDP52(10-126)/NAP1(33-75) complex (2.2 or 1.4 mg/ml in 20 mM Tris-HCl, 100 mM NaCl, 1 mM DTT, 1 mM EDTA at pH 7.5), and TAX1BP1(1-121)/NAP1(33-75) complex (20 or 10 mg/ml in 20 mM Tris-HCl, 100 mM NaCl, 1 mM DTT, 1 mM EDTA at pH 7.5) were grown from 0.2 M sodium malonate buffer at pH 7.0, 20% (w/v) polyethylene glycol 3350, and 0.1 M HEPES buffer at pH 7.5, 4% (w/v) polyethylene glycol 8000, respectively. Before diffraction experiments, appropriate glycerol was added as the cryo-protectant. X-ray data sets were collected at the beamline BL17U1 or BL19U1 of the Shanghai Synchrotron Radiation Facility (3). The diffraction data were processed and scaled using HKL2000 (4).

The phase problem of NDP52(10-126) was solved by the molecular replacement method using the modified structure of NDP52(21-141) (PDB ID: 3VVV) with PHASER (5). While, the phase problems of NDP52(10-126)/NAP1(33-75) complex and TAX1BP1(1-121)/NAP1(33-75) complex were solved by the molecular replacement method using our determined structures of NDP52(10-126) and NDP52(10-126)/NAP1(33-75) complex, respectively. All initial structural models were rebuilt manually using COOT (6), and then refined using REFMAC (7), or PHENIX (8). The qualities of the final model were validated by MolProbity (9). The final refinement statistics of solved structures in this study were listed in ***SI Appendix*** Table S1**.** All the structural diagrams were prepared using the program PyMOL (http://www.pymol.org/).

Co-immunoprecipitation assay. HEK293T cells transiently expressing proteins were harvested, washed with PBS buffer, and lysed for 1 hour at 4 °C in lysis buffer containing 50 mM Tris-HCl (pH 7.8), 50 mM NaCl, 0.4% NP-40, 0.5 mM PMSF and protease inhibitor cocktail (AMRESCO). Lysates were centrifuged, and then supernatants were incubated with appropriate antibody pretreated rProtein G Agarose (Invitrogen) for 3 hours under rotation at 4 °C. Precipitated proteins were washed with lysis buffer for 5 times, and then collected by brief centrifugation. Subsequently, the precipitated proteins were resolved in SDS-PAGE gel and detected by immune-blotting using a chemical luminescence-based detection method.

Cell culture, transfection and fluorescence imaging. HeLa cells were cultured in Dulbecco's modified Eagle's medium (DMEM, Invitrogen) supplemented with 10% fetal

bovine serum (FBS, Invitrogen). Co-transfections of GFP-NAP1 and mCherry-NDP52 or related mutant plasmids were performed with Lipofectamine 2000 (Invitrogen) according to the manufacturer's instructions. After 48 hours, cells were fixed with 4% paraformaldehyde and punched with 0.2% Triton X-100/PBS, and the nuclei were visualized by staining with DAPI. The cell images were captured and analyzed using the TCS SP5 microscope equipped with LAS X software (Leica, Inc.). Particularly, the Pearson's correlation of co-localization was performed using the LAS X software based on a randomly selected region that roughly contains one co-transfected HeLa cell. The statistical data represent mean±s.d. of >30 analyzed cells (selected regions). The unpaired Student t-test analysis was used to define a statistically significant difference.

SI References

1. Bax A & Grzesiek S (1993) Methodological Advances in Protein Nmr. *Accounts Chem Res* 26(4):131-138.
2. Schuck P (2000) Size-distribution analysis of macromolecules by sedimentation velocity ultracentrifugation and lamm equation modeling. *Biophys J* 78(3):1606-1619.
3. Wang Z*, et al.* (2016) Automatic crystal centring procedure at the SSRF macromolecular crystallography beamline. *Journal of synchrotron radiation* 23(Pt 6):1323-1332.
4. Otwinowski Z & Minor W (1997) Processing of X-ray diffraction data collected in oscillation mode. *Method Enzymol* 276:307-326.
5. Storoni LC, McCoy AJ, & Read RJ (2004) Likelihood-enhanced fast rotation functions. *Acta Crystallogr D* 60:432-438.
6. Emsley P & Cowtan K (2004) Coot: model-building tools for molecular graphics. *Acta Crystallogr D* 60:2126-2132.
7. Murshudov GN, Vagin AA, & Dodson EJ (1997) Refinement of macromolecular structures by the maximum-likelihood method. *Acta Crystallogr D* 53:240-255.
8. Adams PD*, et al.* (2002) PHENIX: building new software for automated crystallographic structure determination. *Acta Crystallogr D* 58:1948-1954.
9. Davis IW*, et al.* (2007) MolProbity: all-atom contacts and structure validation for proteins and nucleic acids. *Nucleic acids research* 35:W375-W383.

SI Figures:

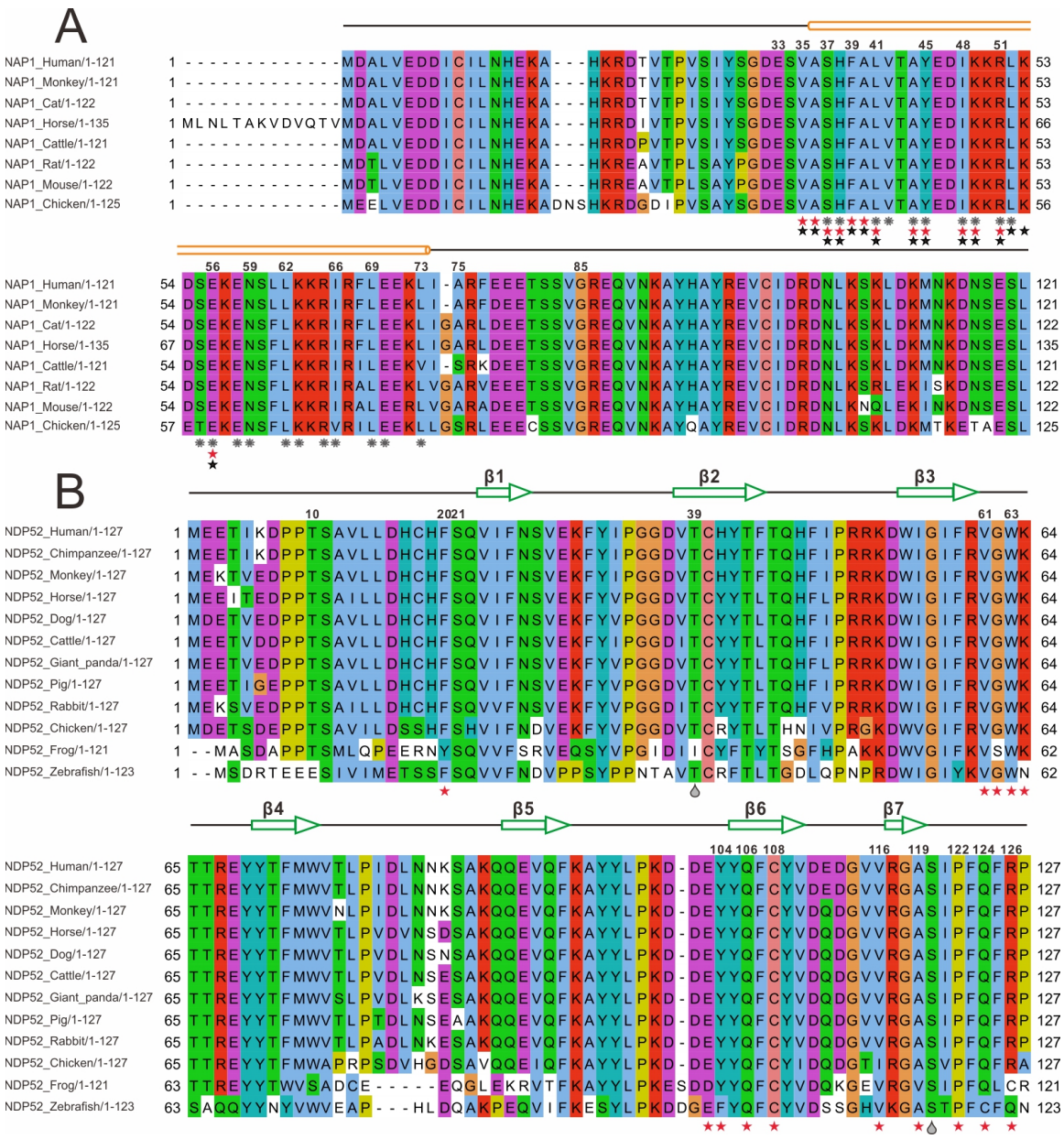

Fig. S1. Sequence alignment analyses of the NAP1 N-terminal coiled-coil region and the SKICH region of NDP52 from different species. (*A*) Structure-based sequence alignment of the N-terminal coiled-coil region of NAP1 from different species. In this alignment, the conserved residues are highlighted by colors using software Jalview2.8.1 (http://www.jalview.org/). The binding interface residues of NAP1 that are important for

the interactions in the NDP52/NAP1 complex and the TAX1BP1/NAP1 complex are highlighted with red and black stars respectively, while the residues that are involved in the dimerization of NAP1 are labeled with grey gears. (***B***) Structure-based sequence alignment of NDP52 SKICH region from different species. The interface residues of NDP52 that are crucial for the interaction with NAP1 in the NDP52/NAP1 complex are highlighted with red stars. The currently reported phosphorylation sites mediated by TBK1 in the SKICH domain of NDP52 are further labeled with grey water-drops.

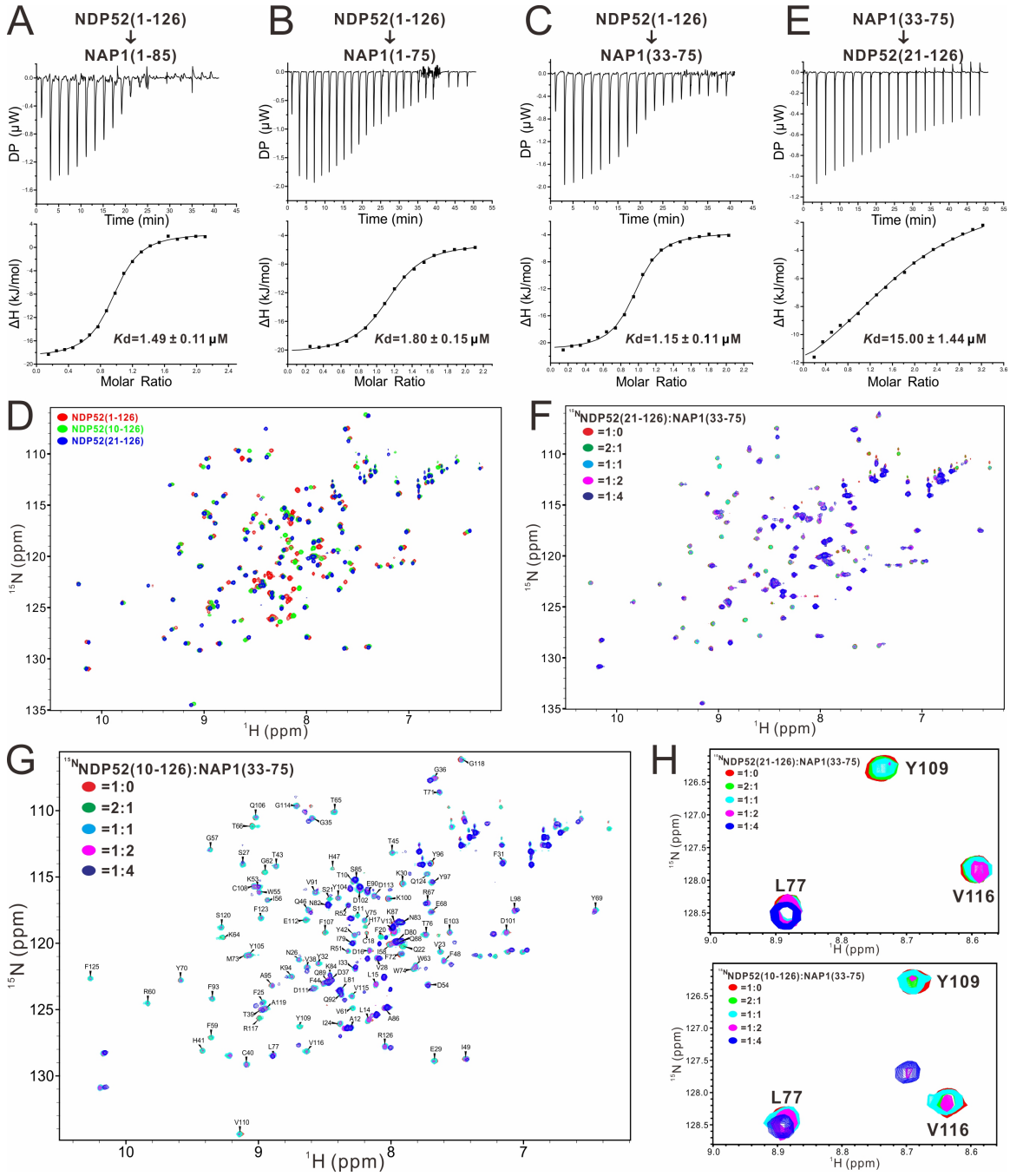

Fig. S2. Biochemical analyses of the interactions between different fragments of NDP52 and NAP1. (*A*-*C*) ITC-based measurements showing the binding affinities of NDP52(1-126) with NAP1(1-85) (***A***), NAP1(1-75) (***B***), and NAP1(33-75) (***C***). The *K*d errors are the fitted errors obtained from the data analysis software, when using the one-site binding model to fit the ITC data. (***D***) Overlay plot of the ^{1}H-^{15}N HSQC spectra of

three NDP52 fragments, NDP52(1-126), NDP52(10-126), and NDP52(21-126). (***E***) ITC-based measurement of the binding affinity of NAP1(33-75) with NDP52(21-126). The *K*d error is the fitted error obtained from the data analysis software, when using the one-site binding model to fit the ITC data. (***F*** and ***G***) NMR-based characterizations of the interactions between NAP1(33-75) and two NDP52 fragments. Superposition plots of the ^{1}H-^{15}N HSQC spectra of ^{15}N-labeled NDP52(21-126) (***F***) or NDP52(10-126) (*G*) titrated with increasing molar ratios of NAP1(33-75) proteins. The peak assignments of the ^{1}H-^{15}N HSQC spectra of NDP52(10-126) are included in panel ***G***. (***H***) Superposition plots of two selected regions of the ^{1}H-^{15}N HSQC spectra of NDP52(10-126) and NDP52(21-126) titrated with increasing molar ratios of the NAP1(33-75) proteins.

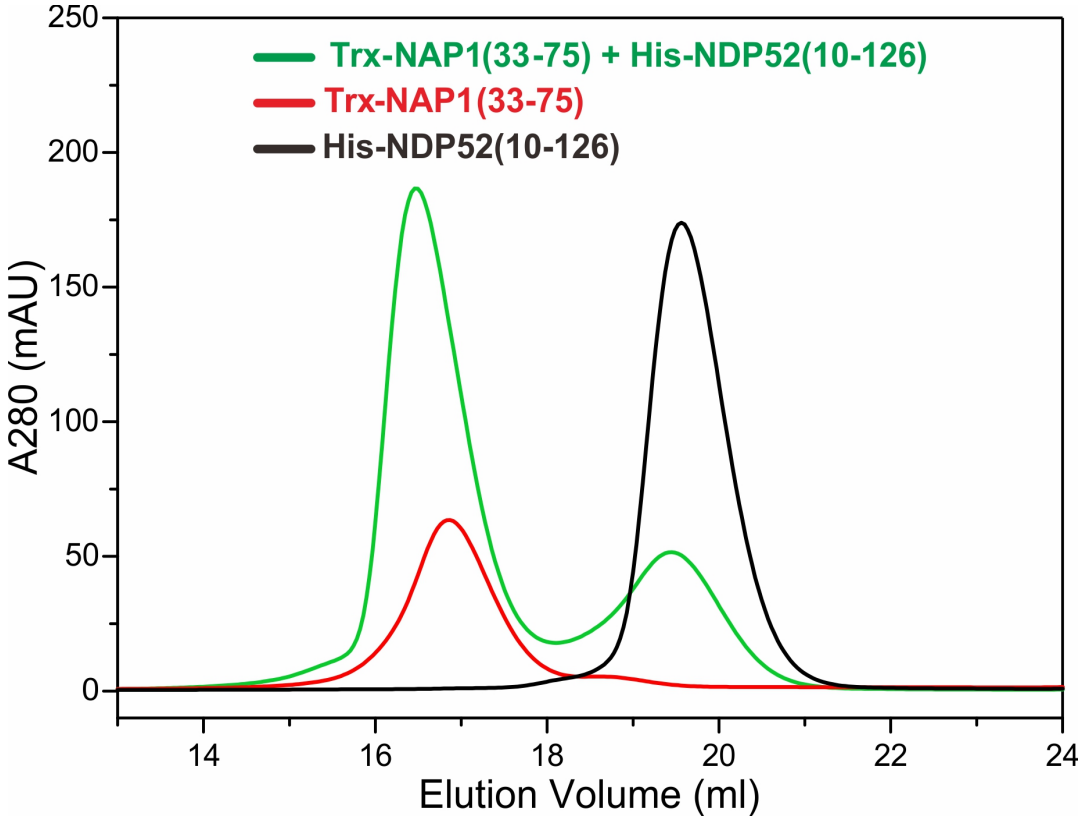

Fig. S3. Analytical gel filtration chromatography analysis of the interaction between

NDP52(10-126) and NAP1(33-75). The analytical gel filtration chromatography analysis showing that NAP1(33-75) can specifically interact with NDP52(10-126), but only forming a single complex peak on the gel filtration profile.

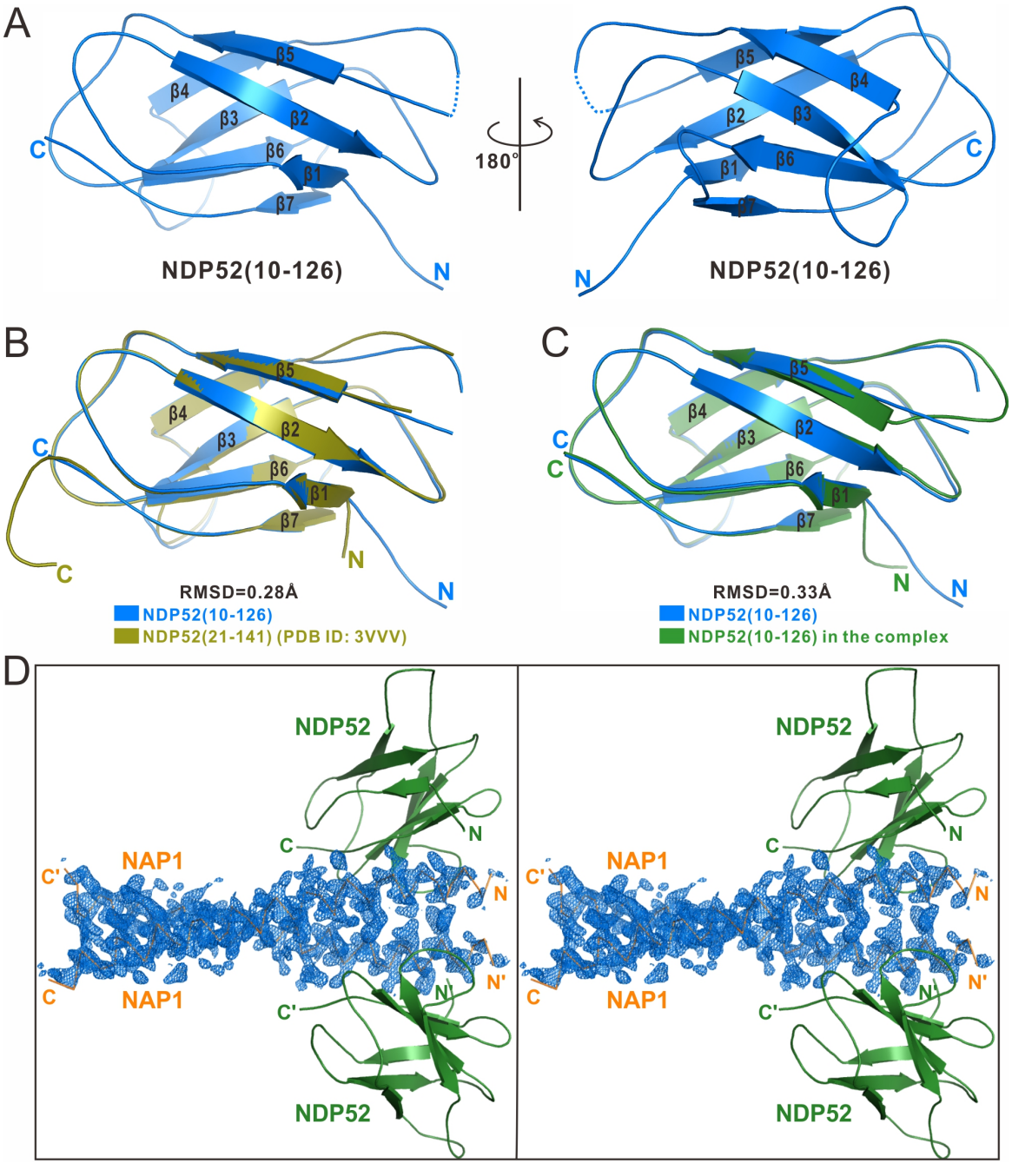

Fig. S4. Structural analyses of the free NDP52(10-126) and the NDP52(10-

126)/NAP1(33-75) complex. (*A*) Ribbon representation showing the overall structure of free NDP52(10-126) determined in this study. (***B*** and ***C***) The ribbon diagram showing the overall structural comparison of the free NDP52(10-126) (marine blue) with the NDP52(21-141) (deep olive) (***B***), or the NDP52(10-126) in the NDP52(10-126)/NAP1(33-75) complex (forest green) (***C***). (***D***) The F_O-F_C map of the NAP1 region in the final structure of the NDP52(10-126)/NAP1(33-75) complex showing that the densities of NAP1(33-75) dimer can be clearly assigned. The electron density map is calculated by omitting the NAP1(33-75) dimer from the final PDB file and contoured at 2.0σ. The two NDP52(10-126) molecules are shown in the cartoon mode, and only the main-chains of NAP1(33-75) dimer are shown in the ribbon mode for simplicity.

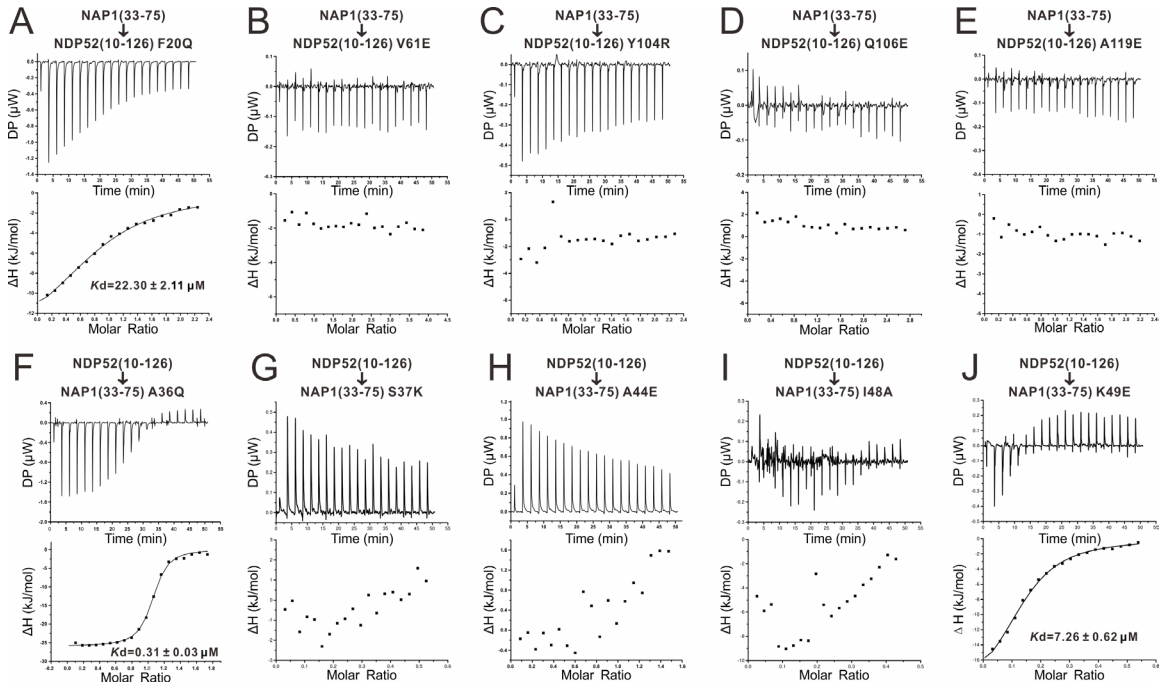

Fig. S5. ITC-based validations of the key interface residues observed in the NDP52(10-126)/NAP(33-75) complex structure. (***A-E***) ITC-based measurements of the binding affinities of NAP1(33-75) with the NDP52(10-126) F20Q mutant (***A***), V61E

mutant (***B***), Y104R mutant (***C***), Q106E mutant (***D***), and A119E mutant (***E***). (***F-J***) ITC-based measurements of the binding affinities of NDP52(10-126) with NAP1(33-75) A36Q mutant (***F***), S37K mutant (***G***), A44E mutant (***H***), I48A mutant (***I***), K49E mutant (***J***). The *K*d errors are the fitted errors obtained from the data analysis software, when using the one-site binding model to fit the ITC data. All these data except that of A36Q mutant confirm the specific interaction between NDP52 and NAP1 observed in our determined complex structure.

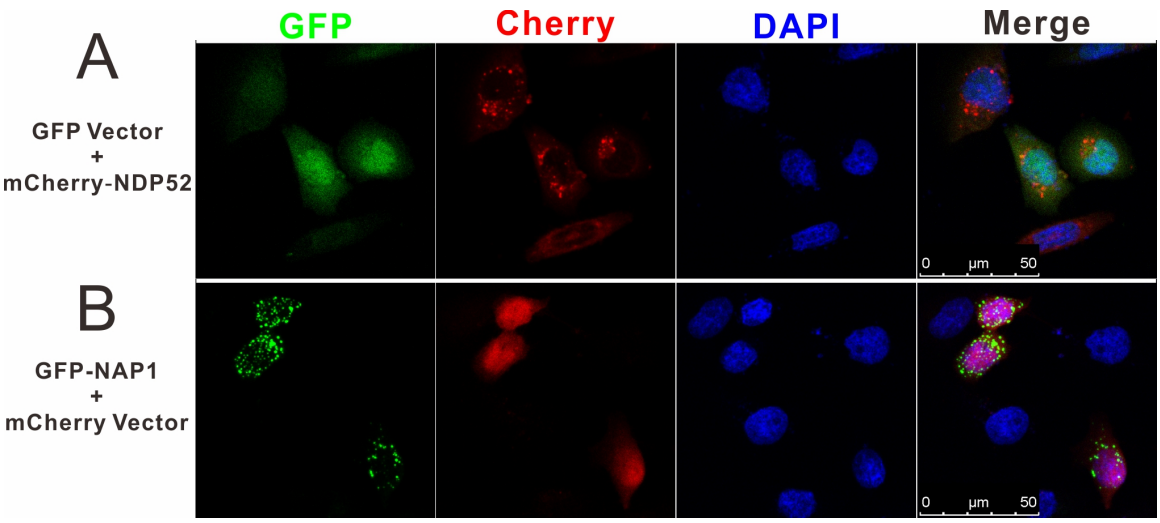

Fig. S6. The cellular localizations of mCherry-tagged NDP52 and GFP-tagged NAP1 with the GFP tag or mCherry tag from the co-transfected empty vector in HeLa cells. (***A***) When co-transfected with the empty GFP vector, the mCherry-tagged NDP52 displays a diffused localization pattern with some puncta, and doesn't co-localize with the GFP tag. (***B***) When co-transfected with the empty mCherry vector, the GFP-tagged NAP1 shows a punctate staining pattern, and doesn't co-localize well with the mCherry tag.

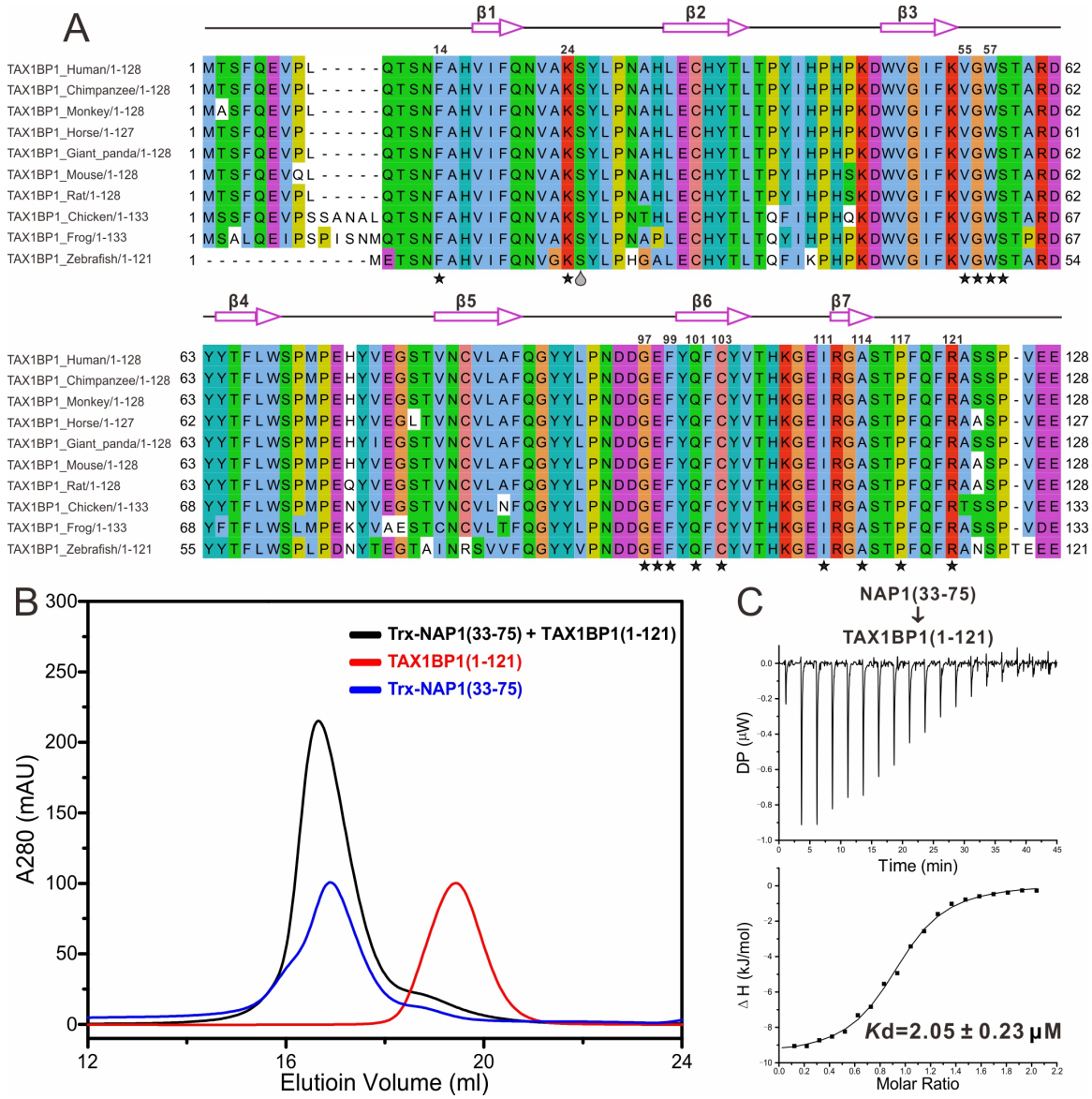

Fig. S7. Sequence and biochemical analyses of the interaction between TAX1BP1 and NAP1. (*A*) Structure-based sequence alignment of TAX1BP1 SKICH region from different species. In this alignment, the conserved residues are highlighted by colors using software Jalview2.8.1 (http://www.jalview.org/). The interface residues that are critical for the interaction with NAP1 in the TAX1BP1(1-121)/NAP1(33-75) complex are highlighted with black stars. The currently known S25 phosphorylation site mediated by the TBK1 kinase in the SKICH domain of TAX1BP1 is further labeled with a grey water-

drop. (***B***) Analytical gel filtration chromatography analyses showing the direct interaction between TAX1BP1(1-121) and NAP1(33-75). (***C***) The ITC-based measurement of the binding affinity of TAX1BP1(1-121) with NAP1(33-75). The *K*d error is the fitted error obtained from the data analysis software, when using the one-site binding model to fit the ITC data.

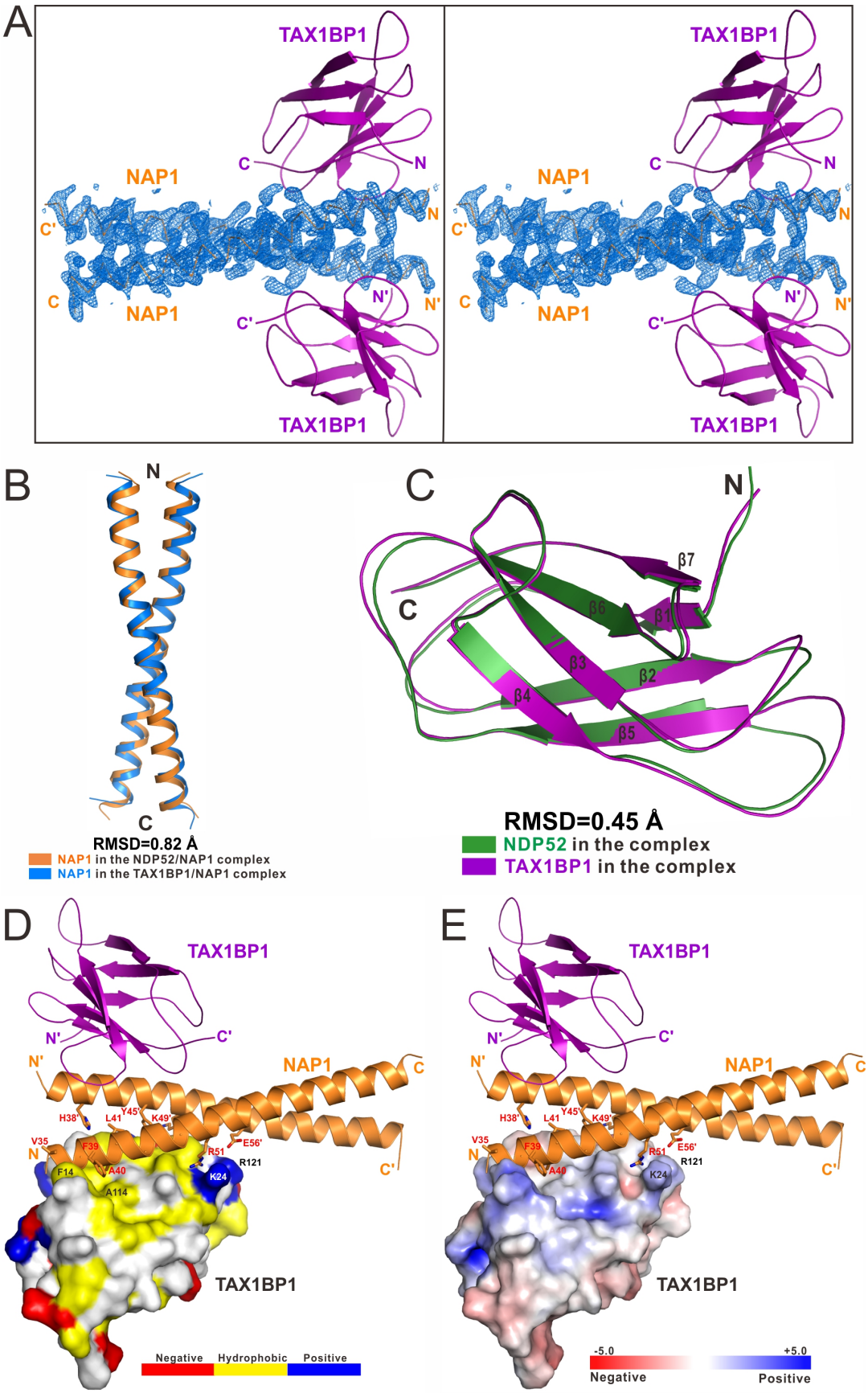
A
TAX1BP1
NAP1
C
N
C'
N
C
NAP1
N'
N'
C'
TAX1BP1
TAX1BP1
NAP1
C
N
C'
N
C
NAP1
N'
N'
C'
TAX1BP1
B
N
C
RMSD=0.82 Å
NAP1 in the NDP52/NAP1 complex
NAP1 in the TAX1BP1/NAP1 complex
C
N
β7
C
β6
β1
β3
β2
β4
β5
RMSD=0.45 Å
NDP52 in the complex
TAX1BP1 in the complex
D
TAX1BP1
N'
C'
N'
NAP1
C
H38'
L41
Y45'
K49'
V35
N
F39
R51
E56'
R121
F14
A40
K24
A114
C'
TAX1BP1
Negative
Hydrophobic
Positive
E
TAX1BP1
N'
C'
N'
NAP1
C
H38'
L41
Y45'
K49'
V35
N
F39
R51
E56'
R121
A40
K24
C'
TAX1BP1
-5.0
+5.0
Negative
Positive

Fig. S8. Detailed structural analyses of the TAX1BP1(1-121)/NAP1(33-75) complex. (***A***) The F_O-F_C map of the NAP1 region in the TAX1BP1(1-121)/NAP1(33-75) complex structure. The electron density map is calculated by omitting the NAP1(33-75) from the final PDB file of the TAX1BP1(1-121)/NAP1(33-75) complex and contoured at 2.0σ. The two SKICH domains of TAX1BP1 are shown in the cartoon mode, and only the main-chains of NAP1(33-75) dimer are shown in the ribbon mode for simplicity. (***B***) Ribbon diagram showing the structure comparison of the NAP1(33-75) dimer in the NDP52/NAP1 and TAX1BP1/NAP1 complexes. (***C***) Ribbon diagram showing the comparison of the conformations of NDP52(10-126) and TAX1BP1(1-121) in their complex structures with NAP1. (***D***) The combined surface representation and the ribbon-stick model showing the hydrophobic binding surface between NAP1(33-75) dimer and one TAX1BP1(1-121) molecule. In this drawing, the NAP1 dimer is displayed in the ribbon-stick model, and one of the TAX1BP1 is shown in the ribbon model and the other in the surface view colored by amino acid types. Specifically, the hydrophobic amino acid residues in the surface model of TAX1BP1 are drawn in yellow, the positively charged residues in blue, the negatively charged residues in red, and the uncharged polar residues in gray. (***E***) The combined surface charge representation and the ribbon-stick model showing the charge-charge interactions between TAX1BP1(1-121) and NAP1(33-75) in the complex structure.

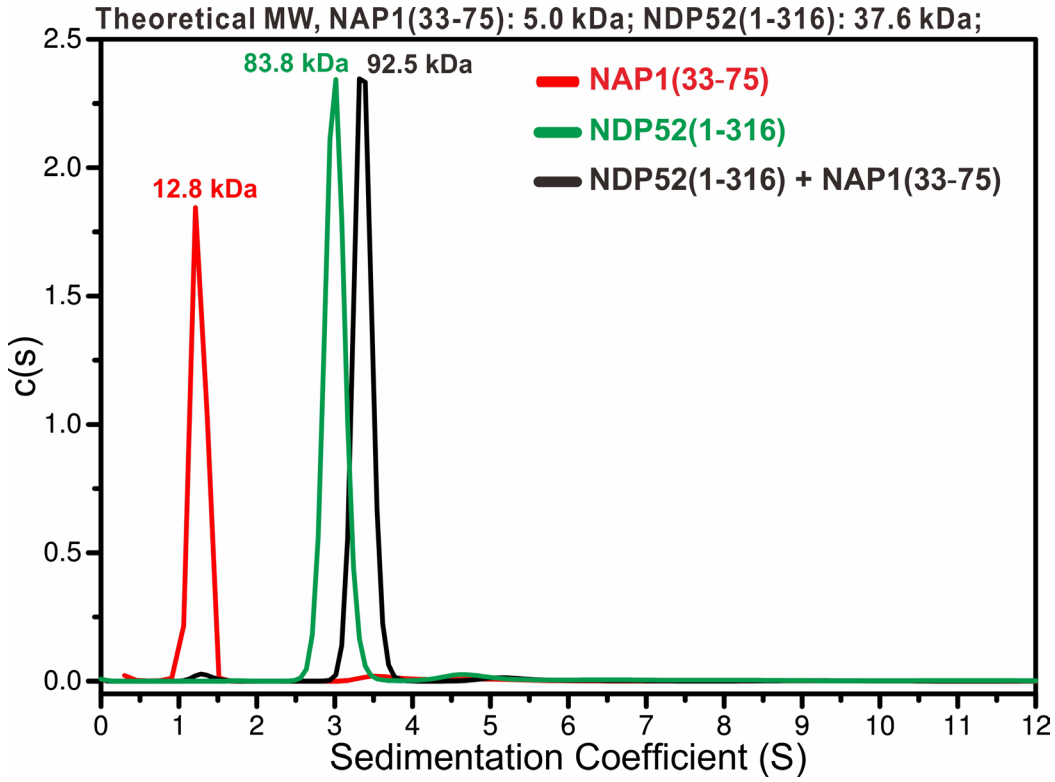

Fig. S9. Analytical ultracentrifugation analysis of the interaction between NDP52(1-316) and NAP1(33-75). The sedimentation velocity analysis showing that the NDP52(1-316) and NAP1(33-75) fragments both form a dimer and interact with each other to form a stable 2:2 stoichiometric complex.

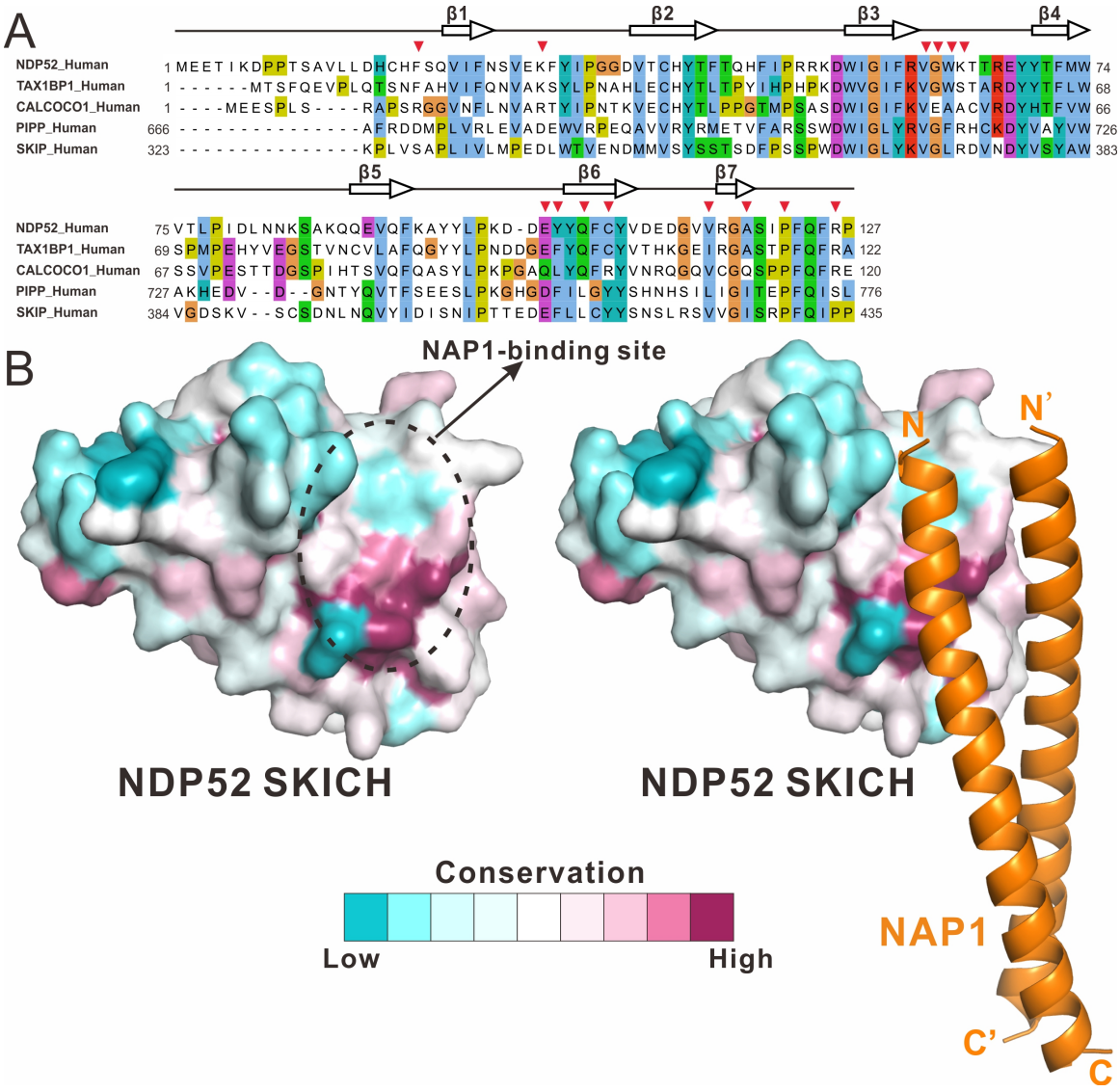

Fig. S10. Sequence and structural analyses of the putative NAP1-binding sites in currently known SKICH domains. (*A*) Detailed structure-based sequence alignment analysis of the SKICH regions of currently known SKICH domain-containing proteins from human species including NDP52, TAX1BP1, CALCOO1, SKIP, and PIPP. In this alignment, the residues that are directly involved in the NAP1 binding are highlighted with red triangles. **(*B*)** Surface representation of NDP52 SKICH (residues 10-126) alone (left panel) or in complex with NAP1 (right panel) showing that the putative NAP1-binding site in known SKICH domain-containing proteins is highly variable. In this

drawing, the surface of NDP52 SKICH is colored according to the sequence conservation based on the amino-acid sequence alignment of different SKICH domains in panel ***A*** using the ConSurf server (http://consurf.tau.ac.il/2016/), and purple and cyan indicate high and low sequence conservation, respectively.

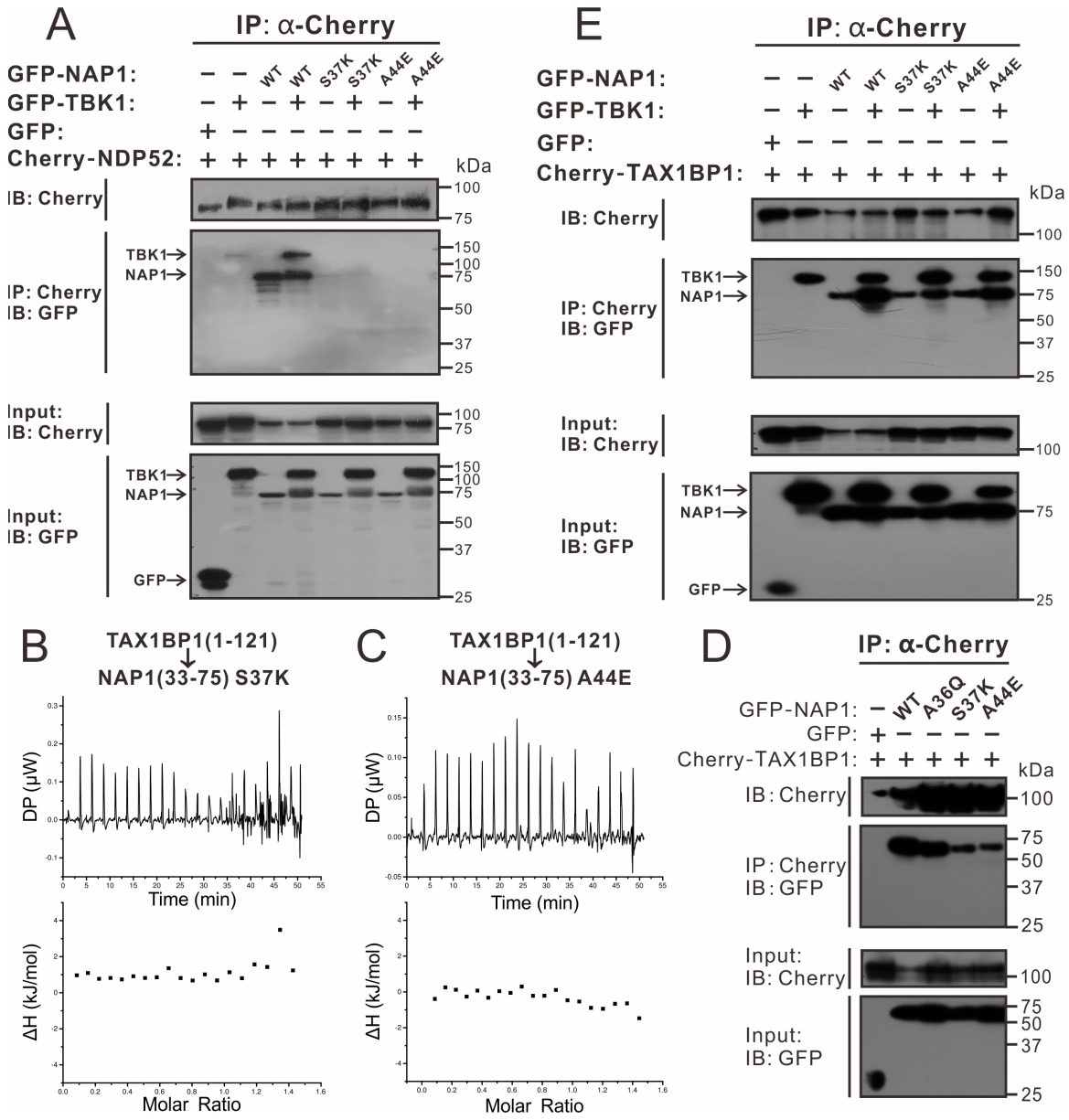

Fig. S11. NDP52 and TAX1BP1 adopt different mechanisms to recruit TBK1. (***A***) A Co-IP assay showing that NDP52 may indirectly associate with the TBK1 kinase through

the adaptor protein NAP1, and mutations of key interface residues of NAP1 such as the S37K and A44E mutations, which were demonstrated to disrupt the specific interaction between NDP52 and NAP1 in this study, essentially abolish the association of NDP52 with TBK1 mediated by NAP1. (***B*** and ***C***) ITC-based measurements of the binding affinities of TAX1BP1(1-121) with the NAP1(33-75) S37K mutant (***B***), and A44E mutant (*C*). (***D***) A Co-IP assay showing that the S37K and A44E mutations of NAP1 can both reduce the interaction between the full-length TAX1BP1 and NAP1 in cells. (***E***) A Co-IP assay showing that TAX1BP1 can directly associate with TBK1, and the NAP1 S37K and A44E mutations that were proved to abolish the interaction between the SKICH domain of TAX1BP1 and NAP1(33-75) *in vitro*, have little effects on the association of TAX1BP1 and TBK1 in cells.

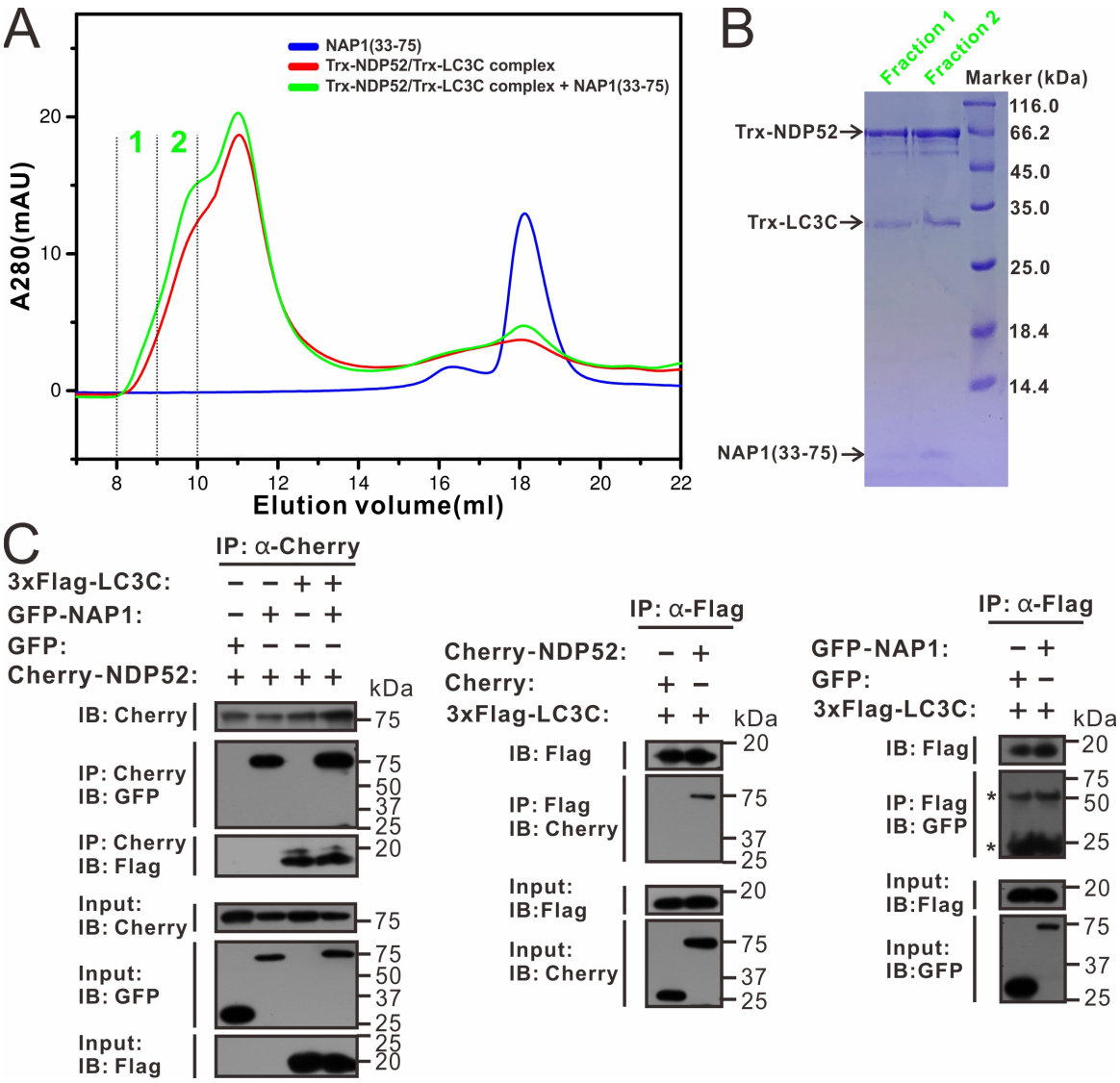

Fig. S12. NDP52 can simultaneously interact with NAP1 and LC3C. (*A*) Analytical gel filtration chromatography analysis of the interaction between the purified NDP52/LC3C complex and the NAP1(33-75) fragment. (*B*) SDS-PAGE combined with Coomassie-blue staining analyses showing the protein components of corresponding fraction 1 and fraction 2 collected from the analytic gel filtration chromatography experiment of the NDP52/LC3C complex mixed with NAP1(33-75) in panel *A* (the gel filtration profile in green). (*C*) Co-IP assays showing that NDP52 can simultaneously bind to NAP1 and LC3C, and NAP1 is unable to directly interact with LC3C in cells. The

two asterisks in the right panel indicate two non-specific bands from the heavy chain and the light chain of the anti-body used in the western blotting analysis.

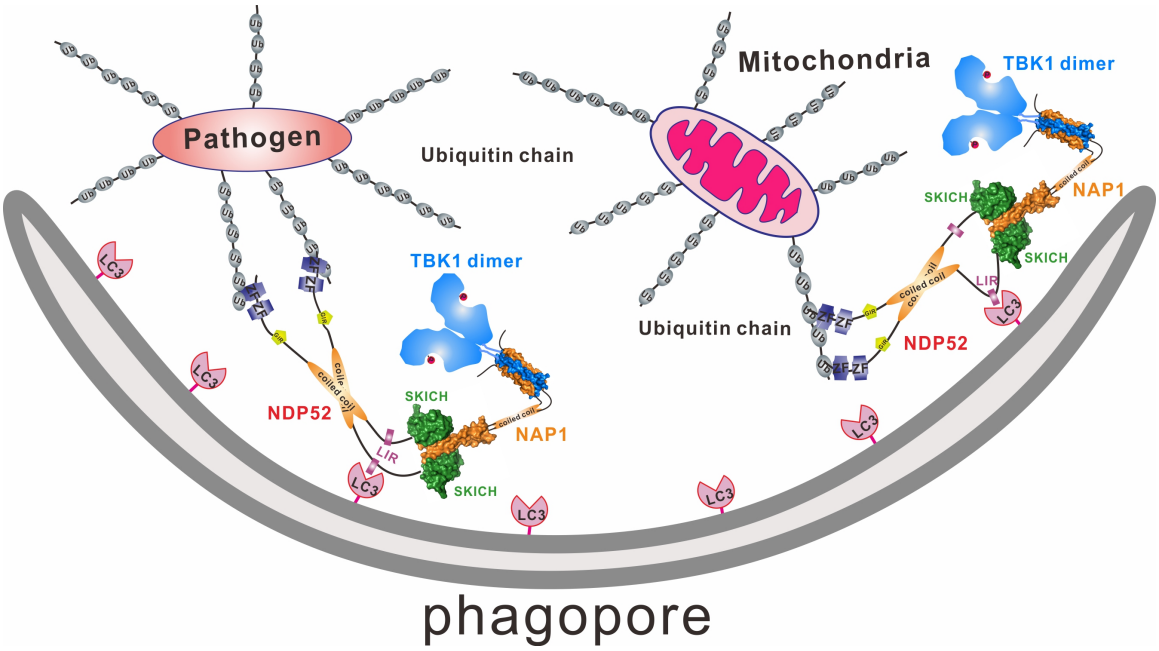

Fig. S13. A proposed model for the NAP1-mediated recruitment of NDP52 to TBK1 as well as the potential regulation of NDP52 by TBK1 in selective autophagy. In this model, NAP1 formed a stable dimer and functioned as an adaptor to associate with the autophagy receptor NDP52 via its N-terminal coiled-coil domain and the TBK1 dimer through its C-terminal TBD domain, thereby forming a hetero-hexamer. Then, the NDP52/NAP1/TBK1 hetero-hexameric complex was recruited to the ubiquitin-decorated mitochondria or pathogen through the secondary ubiquitin-binding ZF domain of NDP52. Finally, the activated TBK1 molecules could directly or indirectly mediate the phosphorylation of NDP52 to regulate its ability to interact with other proteins.

SI Table:

Table S1: Statistics of X-ray crystallographic data collection and model refinements

	NDP52(10-126)	NDP52(10-126)/ NAP1(33-75) complex	TAX1BP1(1-121)/ NAP1(33-75) complex
Data collection			
Wavelength (Å)	0.97946	0.97914	0.97900
Space group	$P3_1$	$C121$	$P63$
Cell dimensions			
a, b, c (Å)	46.50, 46.50, 99.56	113.64, 45.03, 86.68	118.49, 118.49, 64.34
α, β, γ (°)	90, 90, 120	90, 123.77, 90	90, 90, 120
Resolution range (Å)	50.00 - 2.38 (2.43 - 2.38)	72.05 - 2.02 (2.07 - 2.02)	30.00 - 2.30 (2.34 - 2.30)
R_{merge} (%)[a]	8.0 (59.4)	9.6 (63.1)	5.6 (53.0)
$I / \sigma I$	12.49 (1.94)	10.60 (2.30)	36.33 (4.22)
Completeness (%)	90.30 (96.90)	99.50 (99.20)	99.50 (100.00)
$CC_{1/2}$	0.99 (0.60)	0.99 (0.64)	0.99 (0.95)
Redundancy	3.0 (3.1)	3.7 (3.5)	19.8 (16.9)
Refinement			
Resolution (Å)	37.33 - 2.38 (2.72 - 2.38)	40.65 – 2.02 (2.11 – 2.02)	29.62 - 2.30 (2.41 - 2.30)
No. reflections	8378	23688	22878
R_{work} / R_{free} (%)[b]	22.20 (26.86) /26.31 (32.03)	17.03 (26.39) /22.16 (33.04)	18.68 (23.49) /23.32 (32.30)
No. of atoms	1889	2882	2656
Protein	1801	2586	2532
Ligand	24	24	18
Water	64	272	106
Average B-factor (Å^2)	32.06	33.75	62.28
R.m.s.deviations			
Bond lengths (Å)	0.003	0.007	0.008
Bond angles (°)	0.589	0.852	0.853
Ramachandran plot[c]			
Favored region (%)	96.02	98.65	97.64
Allowed region (%)	3.98	1.35	2.36
Outliers (%)	0	0	0

[a] $R_{merge} = \sum|I_i - I_m|/\sum I_i$, where I_i is the intensity of the measured reflection and I_m is the mean intensity of all symmetry related reflections.

[b] $R_{work} = \Sigma||F_{obs}| - |F_{calc}||/\Sigma|F_{obs}|$, where F_{obs} and F_{calc} are observed and calculated structure factors.

$R_{free} = \Sigma_T||F_{obs}| - |F_{calc}||/\Sigma_T|F_{obs}|$, where T is a test data set of about 5% of the total reflections randomly chosen and set aside prior to refinement.

[c] Defined by Molprobity.

Numbers in parentheses represent the value for the highest resolution shell.